Mechanism and Machine Theory 149 (2020) 103746

Contents lists available at ScienceDirect

Mechanism and Machine Theory

journal homepage: www.elsevier.com/locate/mechmachtheory

Research paper

A continuum manipulator for continuously variable stiffness and its stiffness control formulation

Bin Zhao[a], Lingyun Zeng[b], Zhonghao Wu[a], Kai Xu[b,*]

[a] UM-SJTU Joint Institute, Shanghai Jiao Tong University, Shanghai 200240, China
[b] School of Mechanical Engineering, Shanghai Jiao Tong University, Shanghai 200240, China

ARTICLE INFO

Article history:
Received 31 July 2019
Revised 25 October 2019
Accepted 11 December 2019

Keywords:
Continuum manipulator
Constrained bending curvature
Variable stiffness
Cosserat rod
Stiffness control formulation

ABSTRACT

Continuum manipulators can accomplish tasks in cluttered and unstructured environments due to their slenderness. Balancing the workspace and stiffness of the slender continuum manipulator is a primary design concern. Thus, studies have been consistently dedicated to designing continuum manipulators with high or variable stiffness. This paper proposes a 2-segment continuum manipulator with adjustable stiffness based on continuously constrained bending curvature. The manipulator's stiffness is further enhanced via redundant backbone arrangement using the concept of dual continuum mechanism during the design phase. The Cosserat rod theory is used for the kinestatic model to calculate the tip stiffness of the manipulator. A stiffness control formulation utilizes the configuration redundancy of the manipulator to achieve stiffness variation control in a desired direction at a target position. The design concepts, system construction, kinestatic models, stiffness control formulation and experimental validations are presented. The experimental results showed that the tip stiffness of the manipulator can be adjusted in various directions with an enhancement up to 10.83 times of the minimal stiffness, indicating the efficacy of the proposed design and the stiffness control formulation.

1. Introduction

Continuum manipulators, which possess either a continuum structure [1] or an articulated hyper-redundant vertebral structure [2], have shown enhanced dexterity in confined environments and compliant interactions with objects. In medicine, researchers have implemented surgical continuum manipulators with various structures and miniature sizes for different applications. These manipulators can provide advanced instrumentation and be utilized to perform versatile tasks in deep sites through natural orifices or small skin incisions [3]. In field operations, continuum manipulators have the ability to adaptively manipulate and perform a wide variety of tasks [4]. In confined industrial environments, they can perform inspections and other tasks with various exchangeable end-effectors [5–7].

While designing a slender continuum manipulator, a tradeoff between workspace and stiffness should always be of primary consideration. In general, given a desired diameter, the slimmer the manipulator is, the larger the workspace and lower the stiffness are. To enhance or adjust the stiffness, quite a few approaches have been described in recent works:

- In friction-based approaches, the stiffness of the manipulator is essentially adjusted by varying the friction between structural components. Methods for changing the friction include: (i) varying the tension of the actuation tendon

* Corresponding author.
E-mail address: k.xu@sjtu.edu.cn (K. Xu).

https://doi.org/10.1016/j.mechmachtheory.2019.103746
0094-114X/

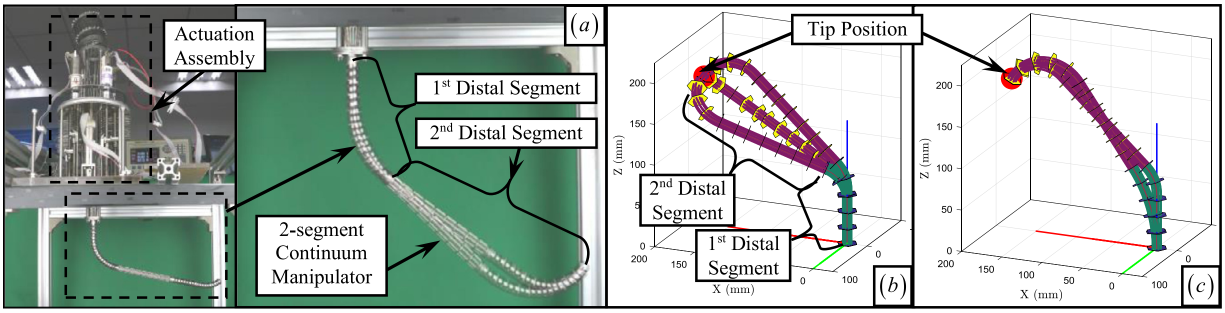

Fig. 1. The 2–segment continuum manipulator: (a) different constrained curvatures overlaid with the same tip position, (b) simulated manipulators with the same tip position and different angles between the two segments' bending planes, and (c) simulated manipulators with same tip position and different constrained curvatures.

[8–11]; (ii) introducing particle jamming [12,13] and layer jamming [14]; and (iii) applying locking mechanisms [15–17]. Varying the tension does not increase the system complexity and facilitate the design compactness, while jamming can substantially increase the stiffness. The friction-based approaches usually need little actuation time to vary the stiffness.
- Continuum manipulators can be designed with active materials including magnetorheological fluids [18], electrorheological fluids [19], shape memory alloys [20], and thermally softened alloys or plastics [21–23]. The manipulator stiffness can be improved by activating these materials. These methods can achieve stiffness variation ratios even up to a few hundreds.
- In approaches based on force sensing, a modified position controller drives a continuum manipulator into different poses to control stiffness upon understanding its mechanics [24–26]. This stiffness variation can also be achieved by a stiffness controller [27] by utilizing the manipulator's intrinsic force sensing capabilities [28–30]. These active stiffness control methods can adjust the stiffness precisely since the stiffness is calculated from on-line force sensing results.

The friction-based approaches face the challenge of actuation hysteresis resulted from the intentionally introduced friction. While using active materials or the force sensing approaches, the additional hardware required for material activation or sensing modalities increases the system complexity. In addition, the response can be slow for thermally activated materials with long switching times (on the order of seconds).

Structural variation, such as by inserting stiffening components [31] or integrating rigid components into the continuum structure [32,33], is another approach used to enhance or adjust the stiffness. This approach usually does not bring actuation hysteresis because the inserted or integrated components only change the structure's elastic bending behaviors. What's more, the inserted components are usually passive. It requires less change to the manipulator structures. Hence, this paper presents a design of a continuum manipulator with continuously variable stiffness. As shown in Fig. 1, the prototype is formed by a 2-segment continuum arm and an actuation assembly. Continuously constrained bending curvature of the continuum segments is introduced to achieve stiffness adjustment, while the redundant backbone arrangement would further enhance the manipulator's stiffness during the design phase.

To describe and control the stiffness of the proposed manipulator, a kinestatic model should be applied. Cosserat rod theory is utilized to calculate the deflected shape and stiffness of the continuum manipulator. Then a stiffness control formulation is proposed to drive the manipulator to the desired tip position and control its tip stiffness. In this particular study, the tip stiffness is quantified as the stiffness along a specific direction, as in Table 1 in Section 4. Since the 2-segment manipulator possesses actuation redundancy for reaching a spatial point, the stiffness control formulation utilizes the redundancy to control tip stiffness while reaching different tip positions by constraining each segment's bending curvature and varying the angle between the segments' bending planes, as shown in Fig. 1(b)–(c).

The contributions of this paper are thus the design of the continuum manipulator and the stiffness control formulation. The joint chain is the key design component that enables the overall idea. A preliminary version of this paper was presented at a conference [34]. In this current paper, the kinestatic model and the entire stiffness control formulation are newly proposed. Moreover, the experimental characterization results are reported to demonstrate the effectiveness of the proposed design and stiffness control formulation.

The findings in this paper can be applied to control or adjust the stiffness of the continuum manipulator to adapt to different operating conditions. The continuum manipulator can reduce its stiffness to accomplish compliant insertions into constrained environments. The low stiffness of the continuum manipulator can prevent damage to the environment and the manipulator. When the manipulator is deployed, it needs enhanced stiffness to perform desired tasks. Hence, continuum manipulators with adjustable stiffness can be more effective in a greater range of applications.

The paper is organized as follows. The design concepts are introduced in Section 2, while Section 3 shows the prototype design and the system construction. The kinematic model is presented in Section 4. Section 5 describes the Cosserat rod theory and stiffness control formulation. Section 6 presents the experiments with the conclusions summarized in Section 7.

Table 1
Nomenclature.

Symbol	Definition
I	Index of the curvature-constraining segments, $i = = 1$ or 2.
J	Index of the backbones, $j = = 1, 2, \ldots, 8$.
l_{bi}	Length of the ith curvature-constraining segment
l_{ci}	Effective segment length (bent portion length) of the ith curvature-constraining segment
l_{total}	Total length of the 2-segment manipulator: $l_{total} = l_{b1} + l_{b2}$
l_r	Length of the rigid portion of DS-2
S	Arc length along the virtual central backbone
ρ_i	Radius of curvature of the bent portion of the ith curvature-constraining segment
δ_i	A right-handed rotation angle from $\hat{\mathbf{y}}_{ip}$ about $\hat{\mathbf{x}}_{ic}$ to a ray passing through the virtual central backbone and the first backbone
δ_d	$\delta_d = \delta_2 - \delta_1$ is the angle between the two segments' bending planes
θ_t	Bending angle of the ith curvature-constraining segment
$\boldsymbol{\psi}_i$	$\boldsymbol{\psi}_i \equiv [\theta_i\ \delta_i\ \rho_i]^T$ is the configuration space of the ith curvature-constraining segment
$\boldsymbol{\psi}$	$\boldsymbol{\psi} \equiv [\boldsymbol{\psi}_1{}^T\ \boldsymbol{\psi}_2{}^T]^T$ is the configuration space of the 2-segment manipulator
$\boldsymbol{\psi}_p$	$\boldsymbol{\psi}_p \equiv [\theta_1\ \delta_1\ \theta_2]^T$ is the position control space of the 2-segment manipulator
$\boldsymbol{\psi}_s$	$\boldsymbol{\psi}_s \equiv [\delta_d\ \rho_1\ \rho_2]^T$ is the stiffness control space of the 2-segment manipulator
$\boldsymbol{\psi}_c$	$\boldsymbol{\psi}_c \equiv [\boldsymbol{\psi}_p{}^T\ \boldsymbol{\psi}_s{}^T]^T$ is the control space of the 2-segment manipulator
${}^{ib}\mathbf{p}_{ie}$, ${}^{ib}\mathbf{R}_{ie}$	Position and orientation of $\{ie\}$ in $\{ib\}$ obtained from the kinematics
${}^{1b}\mathbf{p}_{2e}^{target}$	Target tip position of the stiffness control formulation
${}^{1b}\mathbf{v}_2$	Linear velocity at the tip of the 2-segment manipulator
v_{lim}	Tip velocity limit
$\mathbf{J}_{i\mathbf{v}\boldsymbol{\psi}}$, $\mathbf{J}_{i\omega\boldsymbol{\psi}}$	Linear and angular velocity Jacobian matrices of the ith segment
$\mathbf{J}_{\mathbf{v}\boldsymbol{\psi}}$, $\mathbf{J}_{\mathbf{v}\boldsymbol{\psi}c}$, $\mathbf{J}_{\mathbf{v}\boldsymbol{\psi}p}$, and $\mathbf{J}_{\mathbf{v}\boldsymbol{\psi}s}$	Jacobian matrix of the 2-segment manipulator mapping $\dot{\boldsymbol{\psi}}$, $\dot{\boldsymbol{\psi}}_c$, $\dot{\boldsymbol{\psi}}_p$ and $\dot{\boldsymbol{\psi}}_s$ to ${}^{1b}\mathbf{v}_2$, respectively
${}^{s}\mathbf{f}$	${}^{s}\mathbf{f} = [f\ \alpha\ \beta]^T$ is a virtually applied force at the manipulator's tip for stiffness quantification, expressed in terms of spherical coordinates, where f is the magnitude, α is the inclination angle from $\hat{\mathbf{z}}_{1b}$ and β is the azimuth angle measured from $\hat{\mathbf{x}}_{1b}$.
${}^{1b}\mathbf{f}$	${}^{1b}\mathbf{f} = [f\cdot\sin(\alpha)\cdot\cos(\beta)\ f\cdot\sin(\alpha)\cdot\sin(\beta)\ f\cdot\cos(\alpha)]^T$
${}^{1b}_{\mathrm{f}}\mathbf{p}(s)$, ${}^{1b}_{\mathrm{f}}\mathbf{R}(s)$	Deflected position and orientation of the 2-segment manipulator along its length s, due to the tip force ${}^{1b}\mathbf{f}$
$\mathbf{v}(s)$, $\mathbf{u}(s)$	Change rates of ${}^{1b}_{\mathrm{f}}\mathbf{p}(s)$ and ${}^{1b}_{\mathrm{f}}\mathbf{R}(s)$ along its length s
$\mathbf{m}(s)$,$\mathbf{n}(s)$	Internal moment and force of a Cosserat rod
$\mathbf{K}(s)$	Stiffness matrix of the constitutive model in the Cosserat rod theory relates $\mathbf{u}(s)$ to the internal moment $\mathbf{m}(s)$
$\mathbf{k}_c$, $\mathbf{k}_b$, $\mathbf{k}_r$	Stiffness parameter vectors in the constrained, the bent and the rigid portions of the segment
${}^{1b}_{\mathrm{f}}\mathbf{p}_{2e}$	${}^{1b}_{\mathrm{f}}\mathbf{p}_{2e} \equiv {}^{1b}_{\mathrm{f}}\mathbf{p}(l_{total})$ is the deflected tip position of the 2-segment manipulator
${}^{1b}\mathbf{d}$	${}^{1b}\mathbf{d} = {}^{1b}_{\mathrm{f}}\mathbf{p}_{2e} - {}^{1b}\mathbf{p}_{2e}$ is the tip deflection resulted from the external force ${}^{1b}\mathbf{f}$
$k(\boldsymbol{\psi}, \alpha, \beta)$	tip stiffness of the manipulator along the direction (α, β)
$\mathbf{J}_{k\boldsymbol{\psi}s}$	Jacobian that maps the rate $\dot{\boldsymbol{\psi}}_s$ to the tip stiffness change rate $\dot{k}$

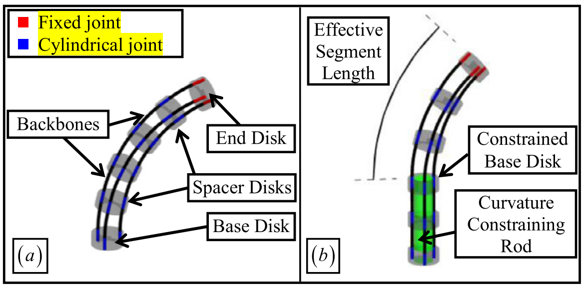

Fig. 2. The bending curvature could be constrained to change stiffness: (a) the continuum segment without the curvature-constraining rod, and (b) the curvature-constrained continuum segment.

2. Design concept and overview

This study presents a design of a 2-segment continuum manipulator to achieve continuously variable stiffness. The design uses the concepts explained in Sections 2.1 and 2.2.

2.1. Constrained bending curvature

As shown in Fig. 2, the first concept is to constrain a continuum segment's bending curvature.

The continuum segment is formed of a base disk, a few spacer disks, an end disk, and several backbones, as illustrated in Fig. 2(a). These backbones are attached to the end disk and actuated to slide in the spacer disks' holes and bend the segment.

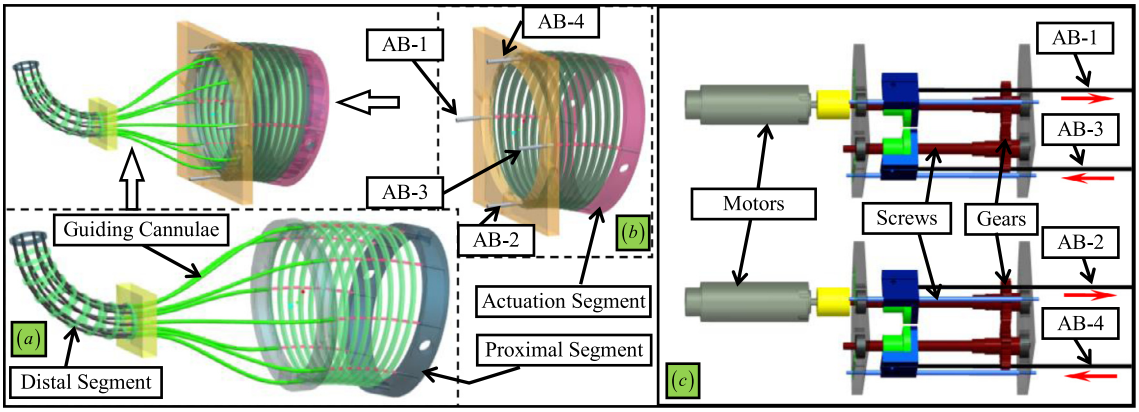

Fig. 3. A dual continuum mechanism assembled with the actuation segment: (a) a dual continuum mechanism formed by a distal segment and a proximal segment, (b) an actuation segment, and (c) two actuation modules for driving the actuation segment.

The proposed concept is that the rigid curvature-constraining rod is inserted to alter the effective segment length (bent portion length), as shown in Fig. 2(b). This concept is based on the idea that a shorter cantilever beam would be stiffer.

Please note that the role of the curvature-constraining rod differs from that of the stiffening rod in [31], since the stiffening rod does not vary the effective segment length. In [32], the continuum segments are serially connected with rigid links, and the effective lengths of segments are not changed. Furthermore, the role of the curvature-constraining rod here is also different from that in [2], in which bending was constrained to generate different kinematics, instead of stiffness.

It should be mentioned that the effective segment length can be continuously changed by the insertion of a rod because there is a continuous surface incorporated between the constraining rod and the disks. The continuous surface would also facilitate rod insertion, as explained in Section 3.1.

2.2. Redundant backbone arrangement

As shown in Fig. 3, the second concept is to utilize the dual continuum mechanism, which can also enhance the stiffness.

Referring to Xu et al. [35], a dual continuum mechanism is formed of a distal segment (DS), a proximal segment (PS), and a few guiding cannulae. These segments' structures are similar to that of the continuum segment shown in Section 2.1. The backbones of DS and PS are connected and routed through the cannulae. Since a similar structure and the same backbone arrangement of the DS and the PS are used, bending the PS causes the DS to bend in the opposite direction. As shown in Fig. 3, to actuate the dual continuum mechanism, the PS should be assembled into an actuation segment (AS). There are four actuation backbones (AB) in the actuation segment, and these ABs are pushed and pulled by two actuation modules. Thus, as shown in Fig. 3(c), only two actuation DoFs are needed to bend the AS, resulting in the bending of the DS, regardless of the number of backbones in the dual continuum mechanism. Furthermore, a multi-segment continuum arm can be formed by serially connecting DSs bent by PSs and ASs.

Stiffness enhancement is achieved by designing the DS with various lengths, sizes and redundant backbone arrangements. For example, the DS can be designed with a minimum of three backbones or a large number of backbones. The latter would obviously enhance the stiffness of DSs, as shown in a previous study [33]. Hence, the redundant backbone arrangement of DS would enhance its stiffness.

3. Design descriptions

The continuum manipulator consists of two distal segments and an actuation assembly that contains two proximal segments. The actuation assembly bends the distal segments via the proximal segments, as well as changes the effective lengths of the DSs. The manipulator and the control infrastructure are described in detail as follows.

3.1. Distal segments with constrained curvature

As in Fig. 4(a), the DS-2 is serially connected to the DS-1. The detailed schematic is shown in Fig. 4(b). As shown in Fig. 5, the arm is actuated by two PSs. The DSs are bent by the PSs, as introduced in Section 2.2.

There are eight nitinol backbones in each DS. As shown in Fig. 4(a), the spacer disks are attached inside a helical strip. The helical strip keeps the spacer disks separate. The spacer disks are welded outside a stainless braided tube. The stainless braided tube is flexible enough to be bent and provides a continuous surface for rod insertion to continuously change the effective segment length.

The design utilizes the two concepts for stiffness variation and stiffness enhancement as presented in Section 2.

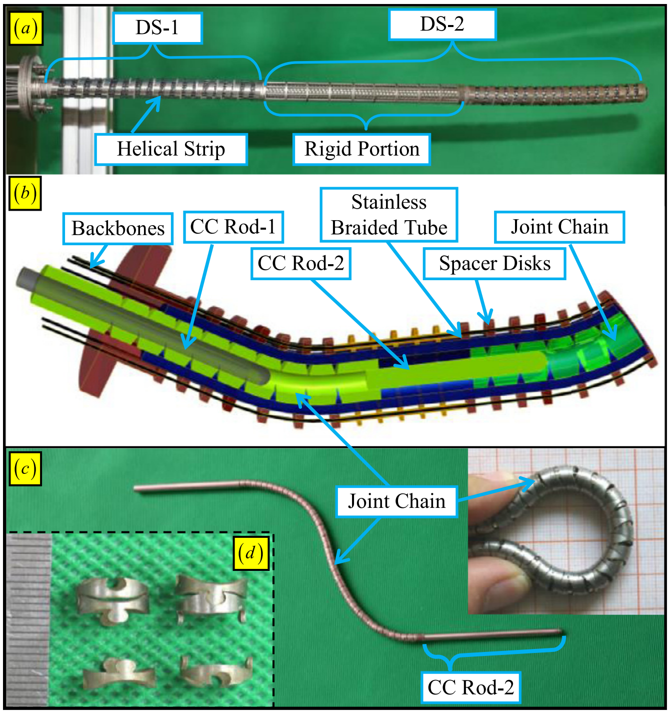

Fig. 4. The distal segments with constrained curvature: (a) the prototype, (b) the schematic, (c) the CC rod-2 with the joint chain, and (d) the fabricated links.

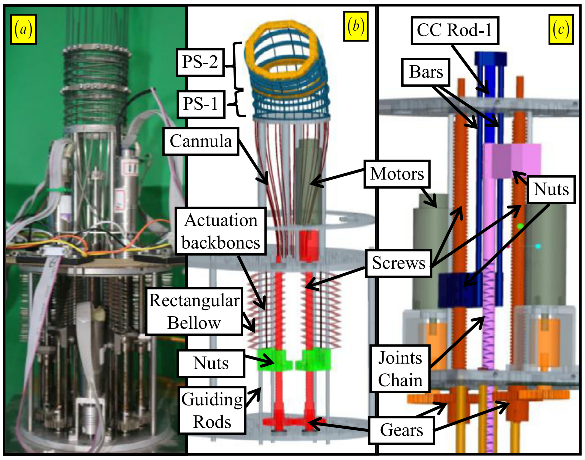

Fig. 5. The actuation assembly for the 2-segment manipulator: (a) the prototype, (b) the PS actuating assembly, and (c) the CC rod actuating assembly.

The first is the dual continuum mechanism. The DSs possess a redundant backbone arrangement to enhance the stiffness. Stiffness of a segment can be enhanced 4 times by increasing the number of backbones from 3 to 18, as shown in a previous study [33]. It is expected that similar stiffness enhancement can be achieved here. Using this stiffness enhancement concept, a continuum segment's stiffness cannot be adjusted once the manipulator is built.

The second concept involves inserting rigid rods to alter the effective segment length of DSs. As depicted in Fig. 4(b), the curvature-constraining rod of the DS-1 is called CC rod-1, while the rod inside DS-2 is called CC rod-2.

A key design for constraining the bending curvature of DS-2 is to allow CC rod-2's insertion into DS-2 without affecting the bending of DS-1. A joint chain (as in Fig. 4(c)) was applied, and it has high axial structural rigidity and very low flexural rigidity such that it can transmit translation but does not affect the bending of DSs. The joint chain is formed by links. As shown in Fig. 4(d), the links are cut from a stainless-steel tube via electrical discharge machining.

Table 2
Parameters of the prototype.

l_{b1}	l_{b2}	l_{total}	l_r	l_{ci}	θ_i	δ_i	ρ_i
100 mm	215 mm	315 mm	115 mm	$\in$ [0 mm, 100 mm]	$\in [0°,135°]$	$\in [0°,360°)$	$\in [40,+\infty]$

As in Fig. 4(c), the CC rod-2 is connected with the joint chain such that the actuation assembly inserts CC rod-2 via the joint chain. On the other hand, the CC rod-1 is directly driven by the actuation assembly for DS-1 and translated inside the joint chain. For consistent structures of the DSs, DS-2 integrates a similar joint chain within it, as shown in Fig. 4(b).

As in Fig. 4(b), DS-2′s rigid portion can house the CC rod-2. This rigid portion must be long enough. Thus, CC rod-2 can be used to alter the effective length of DS-2 without affecting the bending of DS-1. The length of rigid portion l_r is detailed in Table 2.

3.2. Actuation assembly

As shown in Fig. 5, the actuation assembly of the 2-segment manipulator consists of the PS actuating assembly and the CC rod actuating assembly.

In this adopted dual continuum mechanism design, the PS and the AS are integrated. Four actuation backbones are actuated to bend the PS, and they are evenly circumferentially attached to the end disk of the PS. The pair of backbones on the opposite sides of end disk passes through cannulae and is fixed on a pair of nuts. Each pair of nuts is driven by coupled screws via a meshing pair of spur gears to generate opposite motion, and the nut and the rectangular bellow move on the guiding rods. The rectangular bellow is applied to prevent the backbones from buckling. The two PSs need four pairs of actuation backbones, nuts and geared lead screws.

As shown in Fig. 5(c), the joint chain is actuated by a lead screw to translate the CC rod-2. The CC rod-1 is connected to a nut via two bars to compactly arrange the motors, while the nut is driven for translation by the lead screw and the motor.

3.3. Control infrastructure

Six servomotors (Maxon DCX22L from Maxon Group) were applied in the actuation assembly: four servomotors were used to drive the PSs, and two servomotors were applied to actuate the CC rods. The servomotors were controlled and driven by six digital controllers (Maxon EPOS2 24/2 from Maxon Group). The desired positions of the servomotors are calculated using a desktop computer according to actuation kinematics and sent to the digital controllers via a CAN (Controller Area Network) bus.

4. Kinematics

Section 4.1 summarizes the coordinates system, kinematic modeling assumptions, and nomenclature. The kinematics of the system is presented in Section 4.2.

4.1. Coordinates system, modeling assumptions, and nomenclature

The nomenclature for describing the continuum manipulator is detailed in Table 1. For the *i*th curvature-constrained segment, the coordinate system is defined as follows and as shown in Fig. 6.

- The base disk coordinate system$\{ib\} \equiv \{\hat{\mathbf{x}}_{ib}, \hat{\mathbf{y}}_{ib}, \hat{\mathbf{z}}_{ib}\}$ is aligned with the base disk. Its origin is located at the base disk's center, while $\hat{\mathbf{x}}_{ib}$ points from its origin to the first backbone.
- The constrained base disk coordinate system$\{ic\} \equiv \{\hat{\mathbf{x}}_{ic}, \hat{\mathbf{y}}_{ic}, \hat{\mathbf{z}}_{ic}\}$ is aligned with a virtual constrained base disk. Its position is changed via the CC rod insertion. $\{ic\}$ is translated from $\{ib\}$ in the $\hat{\mathbf{z}}_{ib}$.
- Bending plane coordinate system-1 $\{ip\} \equiv \{\hat{\mathbf{x}}_{ip}, \hat{\mathbf{y}}_{ip}, \hat{\mathbf{z}}_{ip}\}$ shares its origin with $\{ic\}$ and has the virtual central backbone bent in its XY plane.
- Bending plane coordinate system-2 $\{iu\} \equiv \{\hat{\mathbf{x}}_{iu}, \hat{\mathbf{y}}_{iu}, \hat{\mathbf{z}}_{iu}\}$ is obtained from $\{ip\}$ by a rotation about $\hat{\mathbf{z}}_{ip}$. Its origin is located at the center of the end disk, and its XY plane is aligned with the bending plane of the segment.
- The end disk coordinate system $\{ie\} \equiv \{\hat{\mathbf{x}}_{ie}, \hat{\mathbf{y}}_{ie}, \hat{\mathbf{z}}_{ie}\}$ is attached to the end disk of the *i*th curvature-constrained segment, and $\hat{\mathbf{z}}_{ie}$ is normal to the end disk. $\hat{\mathbf{x}}_{ie}$ points from its origin to the first backbone.

Three kinematic modeling assumptions are used.

- A virtual central backbone can be applied to characterize the shape and length of the continuum segment, as shown in Fig. 6.
- The shapes of the bent portion can be approximately described as circular arcs, referring to Xu and Simaan [36].
- The length of the constrained portion and bent portion can be continuously changed due to curvature-constraining rods insertion.

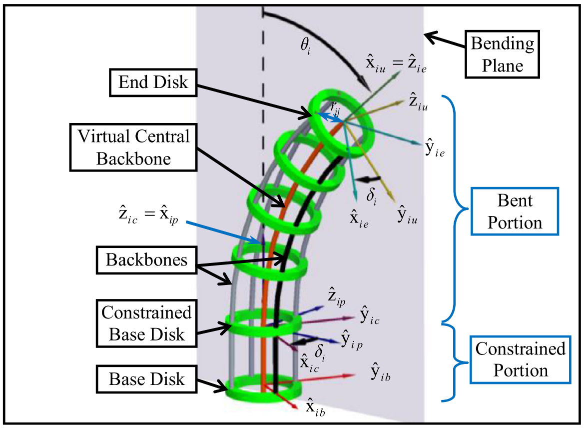

Fig. 6. Coordinates of the curvature-constrained continuum segment.

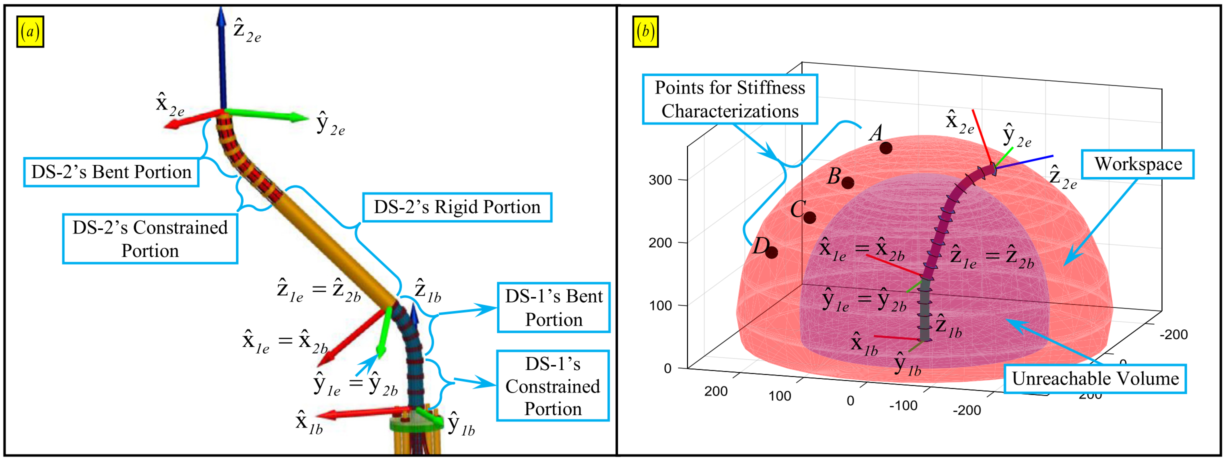

Fig. 7. The 2-segment manipulator: (a) the coordinates, and (b) the workspace.

4.2. Kinematics of the 2-segment arm

The kinematics of a single curvature-constrained segment relies on the insertion of the CC rod because the insertion of the CC rod alters the positions of the constrained base disk and the end disk of a segment, as shown in Fig. 6.

The ith curvature-constrained segment has the configuration space $\boldsymbol{\psi}_i \equiv [\theta_i \ \delta_i \ \rho_i]^T$. The length l_{bi} is constant. The effective segment length l_{ci} can then be represented as $l_{ci} = \theta_i \rho_i$.

Since the base disk of DS-2 is attached to the end disk of DS-1, $\{2b\}$ coincides with $\{1e\}$. The 2-segment arm possesses six DoFs, and it has the configuration space $\boldsymbol{\psi} \equiv [\boldsymbol{\psi}^T{}_1 \ \boldsymbol{\psi}^T{}_2]^T$. The total length of the arm is $l_{total} = l_{b1} + l_{b2}$. As shown in Fig. 7(a), the manipulator's tip position is described as in (1), and the orientation of the end disk is described as in (2).

$$ {}^{1b}\mathbf{p}_{2e} = {}^{1b}\mathbf{p}_{1e} + {}^{1b}\mathbf{R}_{2b}\,{}^{2b}\mathbf{p}_{2e} \tag{1} $$

Where ${}^{1b}\mathbf{R}_{2b} \equiv {}^{1b}\mathbf{R}_{1e}$, and ${}^{ib}\mathbf{R}_{ie}$ and ${}^{ib}\mathbf{p}_{ie}$ are the orientation and position of the end disk of the ith segment, respectively, referring the derivations in to [34].

$$ {}^{1b}\mathbf{R}_{\mathbf{2e}} = {}^{1b}\mathbf{R}_{\mathbf{1e}}\,{}^{1e}\mathbf{R}_{\mathbf{2b}}\,{}^{2b}\mathbf{R}_{\mathbf{2e}} = {}^{1b}\mathbf{R}_{\mathbf{2e}}\,{}^{2b}\mathbf{R}_{\mathbf{2e}} \tag{2} $$

The instantaneous kinematics from $\boldsymbol{\psi}$ to ${}^{1b}\mathbf{p}_{2e}$ can be written as in (3):

$$ {}^{1b}\mathbf{v}_{\mathbf{2}} = \mathbf{J}_{\mathbf{v}\psi}\dot{\boldsymbol{\psi}} \tag{3} $$

Where $\mathbf{J}_{\mathbf{v}\psi} = [\mathbf{J}_{\mathbf{1v}\psi} - [({}^{1b}\mathbf{R}_{\mathbf{2b}}\,{}^{2b}\mathbf{p}_{2e})\times]\mathbf{J}_{\mathbf{1}\omega\psi} \ {}^{1b}R_{2b}\mathbf{J}_{\mathbf{2v}\psi}]$, $[\mathbf{p}\times]$ is the skew-symmetric matrix of the vector $\mathbf{p}$, and $\mathbf{J}_{\mathbf{iv}\psi}$ and $\mathbf{J}_{\mathbf{i}\omega\psi}$ are the linear and angular velocity Jacobian matrices of the ith segment, respectively, referring to Zhao et al. [34].

For the actuation kinematics for driving the backbones of PSs to actuate the DSs to the target $\boldsymbol{\psi}$, please refer to Xu et al. [35].

Table 2 details the parameters of the manipulator. The manipulator's workspace is depicted in Fig. 7(b), while the points (from ${}^{1b}\mathbf{p}_{\mathrm{A}}$ to ${}^{1b}\mathbf{p}_{\mathrm{D}}$) listed in Table 3 for stiffness characterizations are also shown.

Table 3
Points for stiffness characterizations.

${}^{1b}\mathbf{p}_A$	${}^{1b}\mathbf{p}_B$	${}^{1b}\mathbf{p}_C$	${}^{1b}\mathbf{p}_D$
[60 mm 0 mm 300 mm]^T	[120 mm 0 mm 240 mm]^T	[180 mm 0 mm 180 mm]^T	[240 mm 0 mm 120 mm]^T

5. Kinestatic model and stiffness control formulation

In this section, the kinestatic model of the 2-segment continuum manipulator is derived. The Cosserat rod theory is adopted. The 2-segment continuum manipulator is approximated as a single rod with the bending rigidity to be identified, referring to Mahvash and Dupont [24], because the relative motions between various structural members of the slender manipulator is negligible compared with the tip deflection under an external force. This assumption necessarily simplifies the kinestatic model and enables computationally efficient calculation of tip stiffness.

When the manipulator is deployed into an environment for a manipulation, the deflected tip position ${}^{1b}_{\mathbf{f}}\mathbf{p}_{2e}$ and the tip deflection ${}^{1b}\mathbf{d}$ due to the external force ${}^{1b}\mathbf{f}$ can be obtained by solving the Cosserat rod mechanics, as described in Section 5.1. Please note that the external force ${}^{1b}\mathbf{f}$ is a virtual force for quantifying the tip stiffness. The external force ${}^{1b}\mathbf{f}$ can be expressed in a spherical coordinate as ${}^{s}\mathbf{f} = [f\ \alpha\ \beta]^T$, where $f = \|{}^{1b}\mathbf{f}\|$, α is the inclination angle from $\hat{\mathbf{z}}_{1b}$, and β is the azimuth angle from $\hat{\mathbf{x}}_{1b}$. The deflection component parallel to the external force ${}^{1b}\mathbf{f}$ is ${}^{1b}\mathbf{d}_{||} = {}^{1b}\mathbf{d}\cdot{}^{1b}\mathbf{f}/\|{}^{1b}\mathbf{f}\|$. ${}^{1b}\mathbf{d}_{||}$ can be expressed in the spherical coordinate as ${}^{s}\mathbf{d}_{||} = [d\ \alpha\ \beta]^T$, where $d = \|{}^{1b}\mathbf{d}_{||}\|$.

The desired direction for the stiffness adjustment is described by α and β in the spherical coordinate as (α, β). The tip stiffness of the continuum manipulator under the configuration $\boldsymbol{\psi}$ is quantified as $k(\boldsymbol{\psi}, \alpha, \beta) = \|{}^{1b}\mathbf{f}\|/\|\mathbf{d}_{||}\| = f/d$. The target tip stiffness is denoted as $k^{target}(\alpha, \beta)$. As presented in Section 5.2, the stiffness control formulation drives the continuum manipulator to the desired tip position ${}^{1b}\mathbf{p}_{2e}^{target}$ and the control tip stiffness to $k^{target}(\alpha, \beta)$ along the direction (α, β), fully utilizing the manipulator's six actuators.

5.1. Kinestatic model

The 2-segment continuum manipulator is modeled as a single Cosserat rod along the virtual central backbone in the segments. Without an external force, shapes of the segment's bent portion can be approximated circular as in [36]. Then the tip position ${}^{1b}\mathbf{p}_{2e}$ can be calculated using the kinematics model in Section 4.2. The deflected tip position ${}^{1b}_{\mathbf{f}}\mathbf{p}_{2e}$ due to the virtually applied external force ${}^{1b}_{\mathbf{f}}$ (namely ${}^{s}\mathbf{f}$), as well as the tip stiffness $k(\boldsymbol{\psi}, \alpha, \beta)$, can also be calculated as follows.

The manipulator's deflected position ${}^{1b}_{\mathbf{f}}\mathbf{p}(s)$ and orientation ${}^{1b}_{\mathbf{f}}\mathbf{R}(s)$ are functions of the arc length $s \in [0, l_{total}]$. As shown in Fig. 7(a), along the arc length s, the constrained portions of the manipulator are located in $s \in [0, l_{b1}-l_{c1}]\cup[l_{b1}+l_r, l_{total}-l_{c2}]$, while the bent portions are located in $s \in [l_{b1}-l_{c1}, l_{b1}]\cup[l_{total}-l_{c2}, l_{total}]$. The rigid portion of DS-2 is located in $s \in [l_{b1}, l_{b1}+l_r]$.

$\mathbf{v}(s)$ and $\mathbf{u}(s)$, which represent the rates of change of ${}^{1b}_{\mathbf{f}}\mathbf{p}(s)$ and ${}^{1b}_{\mathbf{f}}\mathbf{R}(s)$, are described in (4):

$$\begin{aligned}\frac{d\,{}^{1b}_{\mathbf{f}}\mathbf{p}(s)}{ds} &= {}^{1b}_{\mathbf{f}}\mathbf{R}(s)\mathbf{v}(s)\\ \frac{d\,{}^{1b}_{\mathbf{f}}\mathbf{R}(s)}{ds} &= {}^{1b}_{\mathbf{f}}\mathbf{R}(s)[\mathbf{u}(s)\times]\end{aligned} \tag{4}$$

Where $\mathbf{v}(s)$ is set as $[0\ 0\ 1]^T$, ignoring the shear and longitudinal strains.

Referring to Rucker et al. [37], the equilibrium of a Cosserat rod is formulated with the rates of change of the internal wrench with respect to the arc length s in (5), neglecting the distributed force and moment:

$$\begin{aligned}\frac{d\mathbf{m}(s)}{ds} &= -\left[\frac{d\,{}^{1b}_{\mathbf{f}}\mathbf{p}(s)}{ds}\times\right]\mathbf{n}(s)\\ \frac{d\mathbf{n}(s)}{ds} &= \mathbf{0}\end{aligned} \tag{5}$$

Where $\mathbf{m}(s)$ and $\mathbf{n}(s)$ are the internal moment and force of the rod.

The constitutive model is applied to relate the strains $\mathbf{u}(s)$ and $\mathbf{v}(s)$ to the internal moment $\mathbf{m}(s)$ and inner force $\mathbf{n}(s)$. Since the shear and longitudinal strains are ignored, only the relationship between $\mathbf{u}(s)$ and $\mathbf{m}(s)$ is considered. According to the linear elastic behavior, the internal moment $\mathbf{m}(s)$ at any point s along the rod is given by (6):

$$\mathbf{m}(s) = {}^{1b}_{\mathbf{f}}\mathbf{R}(s)\mathbf{K}(s)(\mathbf{u}(s) - \mathbf{u}^*(s)) \tag{6}$$

Where $\mathbf{K}(s)$ is the stiffness matrix. The 2-segment continuum manipulator has a piecewise stiffness matrix $\mathbf{K}(s)$, as shown in (7):

$$\mathbf{K}(s)=\begin{cases}\mathrm{diag}(\mathbf{k}_c) & s\in[0,\quad l_{b1}-l_{c1}]\cup[l_{b1}+l_r,\quad l_{total}-l_{c2}]\\ \mathrm{diag}(\mathbf{k}_b) & s\in[l_{b1}-l_{c1},\quad l_{b1}]\cup[l_{total}-l_{c2},\quad l_{total}]\\ \mathrm{diag}(\mathbf{k}_r) & s\in[l_{b1},\quad l_{b1}+l_r]\end{cases} \tag{7}$$

Where $\mathbf{k}_\mathrm{c}$, $\mathbf{k}_\mathrm{r}$, and $\mathbf{k}_\mathrm{b}$ are the stiffness parameter vectors of the constrained, the rigid and the bent portions, respectively, as shown in Fig. 7. The stiffness parameters are calibrated in Section 6.2. The original $\mathbf{u}^*(s)$ is given by the kinematic model, and expressed in (8).

$$\mathbf{u}^*(s)=\begin{cases}\frac{1}{\rho_1}{}^{1b}\hat{\mathbf{z}}_{1p} & s\in\left[\ l_{b1}-l_{c1},\quad l_{b1}\ \right]\\ \frac{1}{\rho_2}{}^{1b}\hat{\mathbf{z}}_{2p} & s\in\left[\ l_{total}-l_{c2},\quad l_{total}\ \right]\\ \mathbf{0}_{3\times1} & Otherwise\end{cases} \tag{8}$$

The force ${}^{s}\mathbf{f}=[f\ \alpha\ \beta]^T$ is exerted on the tip of the manipulator along the desired direction $(\alpha,\ \beta)$ for stiffness adjustment. The boundary conditions at the distal tip in (9) are specified from the force ${}^{1b}\mathbf{f}$ that is applied at the manipulator's tip.

$$\begin{aligned}&\mathbf{n}(l_{total})-{}^{1b}\mathbf{f}=\mathbf{0}\\&\mathbf{m}(l_{total})=\mathbf{0}\end{aligned} \tag{9}$$

Because the base of the 2-segment manipulator is fixed, the boundary conditions at the base include the initial position and orientation, as in (10).

$$\begin{aligned}&{}^{1b}_{\mathbf{f}}\mathbf{p}(0)=\mathbf{0}\\&{}^{1b}_{\mathbf{f}}\mathbf{R}(0)=\mathbf{I}\end{aligned} \tag{10}$$

The equations in (4),(5) and (6) can be efficiently solved using the shooting method to obtain the deflected tip position ${}^{1b}_{\mathbf{f}}\mathbf{p}_{2e}\equiv{}^{1b}_{\mathbf{f}}\mathbf{p}_{1b}^{(l_{total})}$, according to Till et al. [38].

With ${}^{1b}_{\mathbf{f}}\mathbf{p}_{2e}$ obtained, the tip deflection is calculated as ${}^{1b}\mathbf{d}={}^{1b}{}_{\mathbf{f}}\mathbf{p}_{2e}-{}^{1b}\mathbf{p}_{2e}$, where ${}^{1b}\mathbf{p}_{2e}$ can be obtained from the kinematics, as described in Section 4.2. Along the desired direction of stiffness adjustment, the deflection parallel to the external force ${}^{1b}\mathbf{f}$ is formulated as ${}^{1b}\mathbf{d}_{||}={}^{1b}\mathbf{d}\cdot{}^{1b}\mathbf{f}/\|{}^{1b}\mathbf{f}\|$ and transformed to the spherical coordinate system as ${}^{s}\mathbf{d}_{||}=[d\ \alpha\ \beta]^T$, where $d=\|{}^{1b}\mathbf{d}_{||}\|$. Hence, the tip stiffness along the direction $(\alpha,\ \beta)$ is denoted as $k(\boldsymbol{\psi},\ \alpha,\ \beta)=f/d$.

5.2. A stiffness control formulation

The proposed manipulator consists of two curvature-constrained segments and possesses six actuators. Hence, the manipulator possesses redundant DoFs to reach a tip position that needs only three DoFs. As shown in Fig. 1(b)–(c), various configurations with the same tip position and different stiffness can be formed.

The tip stiffness of the 2-segment manipulator is influenced by the segments' radii ρ_1 and ρ_2. For the same bending angle, a smaller ρ_i results in a shorter effective segment length and higher tip stiffness, regardless of direction of the external force. Hence, the curvature variation can be used to adjust the tip stiffness of the manipulator.

On the other hand, the continuum segment's stiffness within and outside the bending plane is different, referring to a previous study [33]. Hence, for a desired direction for stiffness adjustment, the bending plane of the segments can also be varied to adjust the stiffness. The angle between the two segments' bending planes is defined as $\delta_d=\delta_2-\delta_1$. The value of δ_d would affect the pose of the manipulator and result in stiffness variation, as shown in Fig. 1(b).

The stiffness control formulation utilizes the redundancy in the configuration space. The stiffness variation of the 2-segment manipulator is achieved by adjusting the stiffness control space vector $\boldsymbol{\psi}_s\equiv[\delta_d\ \rho_1\ \rho_2]^T$, while the position control space vector is $\boldsymbol{\psi}_p\equiv[\theta_1\ \delta_1\ \theta_2]^T$. Hence, the control space of the 2-segment manipulator can be defined as $\boldsymbol{\psi}_c\equiv[\boldsymbol{\psi}_p{}^T\ \boldsymbol{\psi}_s{}^T]^T$, and the tip stiffness along the direction $(\alpha,\ \beta)$ is written as $k(\boldsymbol{\psi}_c,\ \alpha,\ \beta)$.

The instantaneous kinematics from $\boldsymbol{\psi}_c$ to ${}^{1b}\mathbf{p}_{2e}$ can be derived from (3) and described as follows:

$${}^{1b}\mathbf{v}_2=\mathbf{J}_{\mathbf{v}\boldsymbol{\psi}}\begin{bmatrix}\dot{\theta}_1\\ \dot{\delta}_1\\ \dot{\rho}_1\\ \dot{\theta}_2\\ \dot{\delta}_1+\dot{\delta}_d\\ \dot{\rho}_2\end{bmatrix}==\begin{bmatrix}\mathbf{J}^T_{\mathbf{v}\boldsymbol{\psi}}(:,1)\\ \mathbf{J}^T_{\mathbf{v}\boldsymbol{\psi}}(:,2)+\mathbf{J}^T_{\mathbf{v}\boldsymbol{\psi}}(:,5)\\ \mathbf{J}^T_{\mathbf{v}\boldsymbol{\psi}}(:,4)\\ \mathbf{J}^T_{\mathbf{v}\boldsymbol{\psi}}(:,5)\\ \mathbf{J}^T_{\mathbf{v}\boldsymbol{\psi}}(:,3)\\ \mathbf{J}^T_{\mathbf{v}\boldsymbol{\psi}}(:,6)\end{bmatrix}^T\begin{bmatrix}\dot{\theta}_1\\ \dot{\delta}_1\\ \dot{\theta}_2\\ \dot{\delta}_d\\ \dot{\rho}_1\\ \dot{\rho}_2\end{bmatrix}=\begin{bmatrix}\mathbf{J}_{\mathbf{v}\boldsymbol{\psi}p} & \mathbf{J}_{\mathbf{v}\boldsymbol{\psi}s}\end{bmatrix}\begin{bmatrix}\dot{\boldsymbol{\psi}}_p\\ \dot{\boldsymbol{\psi}}_s\end{bmatrix}=\mathbf{J}_{\mathbf{v}\boldsymbol{\psi}c}\dot{\boldsymbol{\psi}}_c \tag{11}$$

Where. $\mathbf{J}_{\mathbf{v}\boldsymbol{\psi}p}=\mathbf{J}_{\mathbf{v}\boldsymbol{\psi}c}(:,1:3)$, and $\mathbf{J}_{\mathbf{v}\boldsymbol{\psi}s}=\mathbf{J}_{\mathbf{v}\boldsymbol{\psi}c}(:,4:6)$.

The stiffness control space $\boldsymbol{\psi}_s$ is varied to change the tip stiffness $k(\boldsymbol{\psi}_c, \alpha, \beta)$. To avoid perturbing the tip position, the rates of change in the stiffness control space $\dot{\boldsymbol{\psi}}_s$ should also satisfy (12), whereas (12) gives (13). The position control space $\boldsymbol{\psi}_p$ should be varied according to (13) to maintain its tip position and generate a desired $\dot{\boldsymbol{\psi}}_s$.

$$\mathbf{0} = \mathbf{J}_{\mathbf{v}\boldsymbol{\psi}p}\dot{\boldsymbol{\psi}}_p + \mathbf{J}_{\mathbf{v}\boldsymbol{\psi}s}\dot{\boldsymbol{\psi}}_s \tag{12}$$

$$\dot{\boldsymbol{\psi}}_p = -\mathbf{J}^+_{\mathbf{v}\boldsymbol{\psi}p}\mathbf{J}_{\mathbf{v}\boldsymbol{\psi}s}\dot{\boldsymbol{\psi}}_s \Rightarrow \Delta\boldsymbol{\psi}_p = -\mathbf{J}^+_{\mathbf{v}\boldsymbol{\psi}p}\mathbf{J}_{\mathbf{v}\boldsymbol{\psi}s}\Delta\boldsymbol{\psi}_s \tag{13}$$

Where $\mathbf{J}^+_{\mathbf{v}\boldsymbol{\psi}s}$ is the pseudo inverse of the Jacobian $\mathbf{J}_{\mathbf{v}\boldsymbol{\psi}p}$.

The rate of change in the stiffness control space $\dot{\boldsymbol{\psi}}_s$ generates a stiffness change rate $\dot{k}$ along the desired stiffness adjustment direction (α, β) according to (14):

$$\dot{k} = \mathbf{J}_{k\boldsymbol{\psi}s}\dot{\boldsymbol{\psi}}_s \tag{14}$$

Where the Jacobian $\mathbf{J}_{k\boldsymbol{\psi}s}$ is computed via a finite difference approach that evaluates the stiffness control vector $\boldsymbol{\psi}_s$: For a given control space $\boldsymbol{\psi}_c$, the tip stiffness $k(\boldsymbol{\psi}_c, \alpha, \beta)$ is calculated first using the Cosserat rod mechanics. Then, $\Delta\boldsymbol{\psi}_c = [\Delta\boldsymbol{\psi}_p{}^T \; \Delta\boldsymbol{\psi}_s{}^T]^T$ is obtained by varying the stiffness control vector $\boldsymbol{\psi}_s$ to get $\Delta\boldsymbol{\psi}_s$ and calculate $\Delta\boldsymbol{\psi}_p$ using (13). Each column of $\mathbf{J}_{k\boldsymbol{\psi}s}$ is computed by varying the control space, re-evaluating the tip stiffness, and dividing the difference in tip stiffness by the increments.

Hence, to generate a desired stiffness change rate $\dot{k}$ and maintain the tip position, the rate of change in the control space $\dot{\boldsymbol{\psi}}_c$ can be obtained according to (15), derived from (13) and (14).

$$\dot{\boldsymbol{\psi}}_c = \begin{bmatrix} -\mathbf{J}^+_{\mathbf{v}\boldsymbol{\psi}p}\mathbf{J}_{\mathbf{v}\boldsymbol{\psi}s}\mathbf{J}^+_{k\boldsymbol{\psi}s} \\ \mathbf{J}^+_{k\boldsymbol{\psi}s} \end{bmatrix}\dot{k} \tag{15}$$

Where $\boldsymbol{J}^+{}_{k\boldsymbol{\psi}s}$ is the pseudo inverse of the Jacobian $\mathbf{J}_{k\boldsymbol{\psi}s}$.

During each iteration of the stiffness control process, the arm is driven toward a target tip position ${}^{1b}\mathbf{p}_{2e}^{target}$ while attempting to reach target tip stiffness $k^{target}(\alpha, \beta)$ in a desired direction (α, β).

First, the desired linear velocity ${}^{1\mathrm{b}}\mathbf{v}_2$ is obtained according to (16). Then, the increment in the position control space $\Delta\boldsymbol{\psi}_p$ is to drive the manipulator towards ${}^{1b}\mathbf{p}_{2e}^{target}$ as in (17).

$${}^{1b}\mathbf{v}_2 = v_{lim}({}^{1b}\mathbf{p}_{2e}^{target} - {}^{1b}\mathbf{p}_{2e}^{current})/\left\| {}^{1b}\mathbf{p}_{2e}^{target} - {}^{1b}\mathbf{p}_{2e}^{current} \right\| \tag{16}$$

Where v_{lim} is a coefficient for limiting the tip velocity.

$$\Delta\boldsymbol{\psi}_p = \mathbf{J}^+_{\mathbf{v}\boldsymbol{\psi}p}\,{}^{1b}\mathbf{v}_2\Delta t \tag{17}$$

Where Δt is the time duration for each iteration.

Second, the desired tip stiffness change rate $\dot{k}$ is obtained according to (18). Then, the increment in the control space $\Delta\boldsymbol{\psi}_c$ is written in (19) according to (15).

$$\dot{k} = k_{lim}(k^{target}(\alpha, \beta) - k(\boldsymbol{\psi}_c, \alpha, \beta))/\left|k(\boldsymbol{\psi}_c, \alpha, \beta) - k^{target}\right| \tag{18}$$

Where k_{lim} is a coefficient for limiting the stiffness change rate.

$$\Delta\boldsymbol{\psi}_c = \begin{bmatrix} -\mathbf{J}^+_{\mathbf{v}\boldsymbol{\psi}p}\mathbf{J}_{\mathbf{v}\boldsymbol{\psi}s}\mathbf{J}^+_{k\boldsymbol{\psi}s} \\ \mathbf{J}^+_{k\boldsymbol{\psi}s} \end{bmatrix}\dot{k}\Delta t \tag{19}$$

During each iteration, the control space $\boldsymbol{\psi}_c$ is updated as in (20):

$$\boldsymbol{\psi}_c \leftarrow \boldsymbol{\psi}_c + \begin{bmatrix} \mathbf{J}^+_{\mathbf{v}\boldsymbol{\psi}p}\,{}^{1b}\mathbf{v}_2 - \mathbf{J}^+_{\mathbf{v}\boldsymbol{\psi}p}\mathbf{J}_{\mathbf{v}\boldsymbol{\psi}s}\mathbf{J}^+_{k\boldsymbol{\psi}s}\dot{k} \\ \mathbf{J}^+_{k\boldsymbol{\psi}s}\dot{k} \end{bmatrix}\Delta t \tag{20}$$

6. Experimental characterizations

It is known from previous studies [39] that there exists a discrepancy between the actual bending angle and the commanded angle of a segment; therefore, motion compensation is necessary for bending the 2-segment manipulator to accurate angles. The motion compensation is presented in Section 6.1. Since the manipulator is modeled as a single Cosserat rod in Section 5.1, the stiffness parameter calibration of the Cosserat rod is presented in Section 6.2 to accurately predict the tip stiffness. The numerical simulations and experimental verifications of the stiffness control formulation are in Sections 6.3 and 6.4, respectively, to demonstrate the efficacy of the proposed design and the stiffness control formulation.

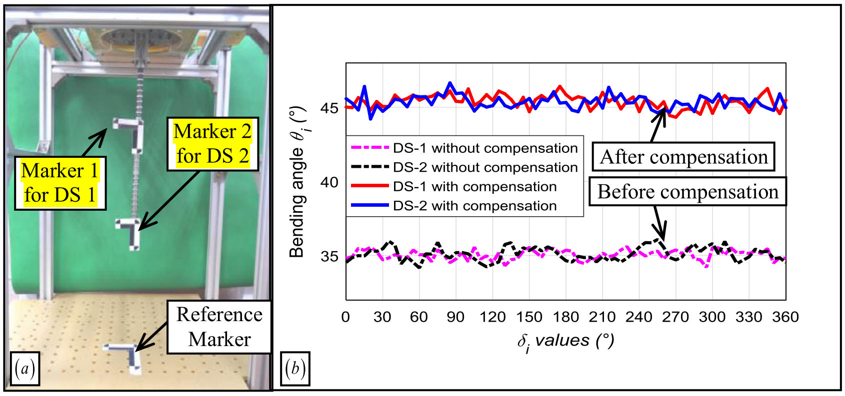

Fig. 8. Motion compensation of the segments: (a) setup of bending measurements, and (b) bending measurements of the DSs before and after compensation.

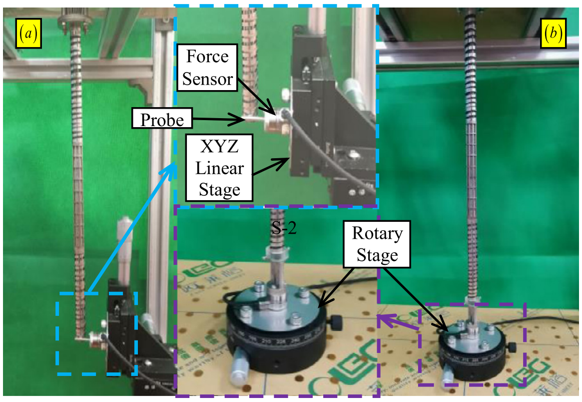

Fig. 9. Experimental setup of stiffness calibration for (a) $\mathbf{k}_{|x,y}$ and (b) $\mathbf{k}_{|z}$.

6.1. Motion compensation

The experimental setup for motion compensation is shown in Fig. 8(a), referring to [39]. Markers are attached to the end disk of DSs. The continuum segments were actuated to bend to $\theta_i = 45°$, with δ_i ranging from 0° to 360° with an interval of 5°. The actual angle can be measured by an optical tracker (Micron Tracker SX60 from Claron Technology Inc.) and plotted in Fig. 8(b).

Then the adopted motion compensation was described as in (21):

$$\tilde{\theta}_i = w_i\theta_i, \quad i = 1, 2 \tag{21}$$

Where the compensation coefficients are $w_1 = 1.280$ and $w_2 = 1.285$ for the two distal segments. For the target θ_i, the compensated $\tilde{\theta}_i$ should be applied to bend the DS.

As plotted in Fig. 9(b), the bending angles fluctuated around the target value after compensation. The compensated bending angle is shown to have errors within 2° from the target angle. The errors can be primarily from two aspects. Firstly, the measurement accuracy of the tracker is about 0.20 mm. The marker is 30 mm long. Then the resultant angle measurement accuracy is calculated to be 0.76°. What is more, there are tolerances assigned in the holes in which the backbones are passed. The tolerances also contribute to the bending errors. Benefiting from the redundant backbone arrangement, there is no need to compensate for δ_i.

6.2. Stiffness parameter calibration

Calibration of the stiffness matrix $\mathbf{K}(s)$ of the Cosserat rod is presented here. As described in (7), $\mathbf{K}(s)$ is a piecewise function composed of the parameters of the constrained, the bent and the rigid portions of the manipulator (a.k.a., $\mathbf{k}_c$, $\mathbf{k}_b$ and $\mathbf{k}_r$). These parameters shall be calibrated.

As shown in Fig. 9, the continuum manipulator was set straight. Then, it was driven to change the bent portion length l_{ci} from 0 mm to 100 mm with an interval of 10 mm. Under each value of l_{ci}, a six-axis force sensor (Nano-17 from ATI

Table 4
Parameters of the numerical experiments.

Δt	v_{lim}	k_{lim}	f	α	β
0.01 s	20 mm/s	1.1 N/mm/s	0.5 N	$\pi/2$ rad	0 rad

Industrial Automation) was used to measure the stiffness of the manipulator. The force sensor can sense the force with a 1/160-N sensing accuracy, and it can also measure the torque with a 1/32-Nmm sensing accuracy.

First, the *xy*-components of the stiffness parameters, $\mathbf{k}|_{x,y}$=$[\boldsymbol{k}_b|_{x,y}\ \boldsymbol{k}_c|_{x,y}\ \boldsymbol{k}_r|_{x,y}]^T$, were calibrated. As shown in Fig. 9(a), the force sensor was applied to sense the exerted force and attached on a *XYZ* linear stage. The probe mounted on the force sensor was first driven by the *XYZ* linear stage to touch the tip of the arm. Then, the tip of the arm is perturbed by the probe in the $\hat{x}_{1b}$ direction. For every 0.5-mm perturbation generated by the *XYZ* linear stage, the force sensor recorded the exerted forces. The measured tip stiffness $k_m(\pi/2,0)$ was obtained by a linear regression between the forces and the perturbations. Then, the predicted stiffness $k(\boldsymbol{\psi},\ \pi/2{,}0)$ was obtained by solving the Cosserat theory equations, as detailed in Section 5.1. Using the measured stiffness and the kinestatic model, an optimization could be formulated as in (22), which involves parameter $\mathbf{k}|_{x,y}$. Then, the *fmincon* function, which is a nonlinear multivariable algorithm implemented in MATLAB, was used to solve this optimization equation using initial values $\mathbf{k}|_{x,y}$=[0.5 1 5] Nm^2, yielding a result of $\mathbf{k}|_{x,y}$=[0.581 2.331 6.962] Nm^2.

$$\mathbf{k}_{|x,y} = \arg\min_{\mathbf{k}_{|x,y}} \left(\frac{1}{n} \sum_{p=1}^{n} \left\| k_m\left(\tfrac{\pi}{2}, 0\right) - k\left(\boldsymbol{\psi}, \tfrac{\pi}{2}, 0\right) \right\| \right) \tag{22}$$

Second, the z-components of the stiffness parameters, $\mathbf{k}|_z = [\mathbf{k}_b|_z\ \mathbf{k}_c|_z\ \mathbf{k}_r|_z]^T$, are calibrated. The 6D force sensor was fixed on the rotary stage and connected with the end disk of the continuum manipulator. As shown in Fig. 9(b), the end disk was rotated by the rotary stage. The exerted torques were measured for every 0.5° rotation. A linear regression between the torque and the rotations gave the torsional stiffness. Then, the predicted torsional stiffness can be obtained by solving the Cosserat theory equations, as detailed in Section 5.1. Similarly in the optimization of $\mathbf{k}|_{x,y}$, the optimization involving $\mathbf{k}|_z$ was applied to minimize the errors between predictions and measurements, and the result of $\mathbf{k}|_z$ is [0.0875 0.366 2.503] Nm^2.

6.3. Numerical experiments of stiffness control formulation

Stiffness control formulation utilizes the redundancy in the configuration space, and the stiffness variation of the 2-segment manipulator is achieved by adjusting the stiffness control space. Different ρ_i and δ_d values lead to different stiffness. To verify the proposed idea, this section presents numerical experiments for three case studies, as shown in Fig. 10.

In these three cases, the simulated manipulator is actuated to the target position and then driven by the stiffness control formulation to control the tip stiffness and maintain the tip position at ${}^{1b}\mathbf{p}_c$. The simulations vary the continuum manipulator from the initial configuration with high stiffness, to the configuration with low stiffness, and back to the original configuration. Case I is simulated to change the radii of curvature ρ_i to vary the tip stiffness and maintain the tip position while keeping δ_d constant. Case II is carried out to vary δ_d to change the tip stiffness and maintaining the tip position while keeping ρ_i constant. In Case III, the stiffness control formulation varies stiffness control space $\boldsymbol{\psi}_s$ to change the tip stiffness. These three cases have the same initial configuration, and the parameters of the numerical experiments are detailed in Table 4.

The results of the three cases are depicted in Fig. 10. The simulations are shown in the first column of Fig. 10, and the poses with high stiffness and low stiffness are presented. The control space variations are shown in the second column of Fig. 10. The tip stiffness variations are shown in the third column of Fig. 10.

Some observations can be made from Fig. 10.

- As shown in Case I, smaller ρ_i (higher curvature) leads to higher tip stiffness. The initial configuration of stiffness control formulation with $\rho_i = 40$ mm possesses the higher tip stiffness, while the configuration with bigger ρ_i has the lower stiffness.
- Varying δ_d also leads to tip stiffness variation, as shown in Case II. Hence, stiffness variation could be achieved by adjusting the control space $\boldsymbol{\psi}_c$, as demonstrated in Case III.
- The stiffness control formulation can maintain the tip position of the manipulator at the desired position, as shown in the simulation, when the control space is varied to change the tip stiffness.

6.4. Stiffness variation within the workspace

The stiffness variation of the proposed continuum manipulator does depend on the positions as well as the manipulator poses within the workspace. The reason is somewhat straightforward: this slender continuum manipulator tends to have higher stiffness in the axial direction and lower stiffness in the lateral direction.

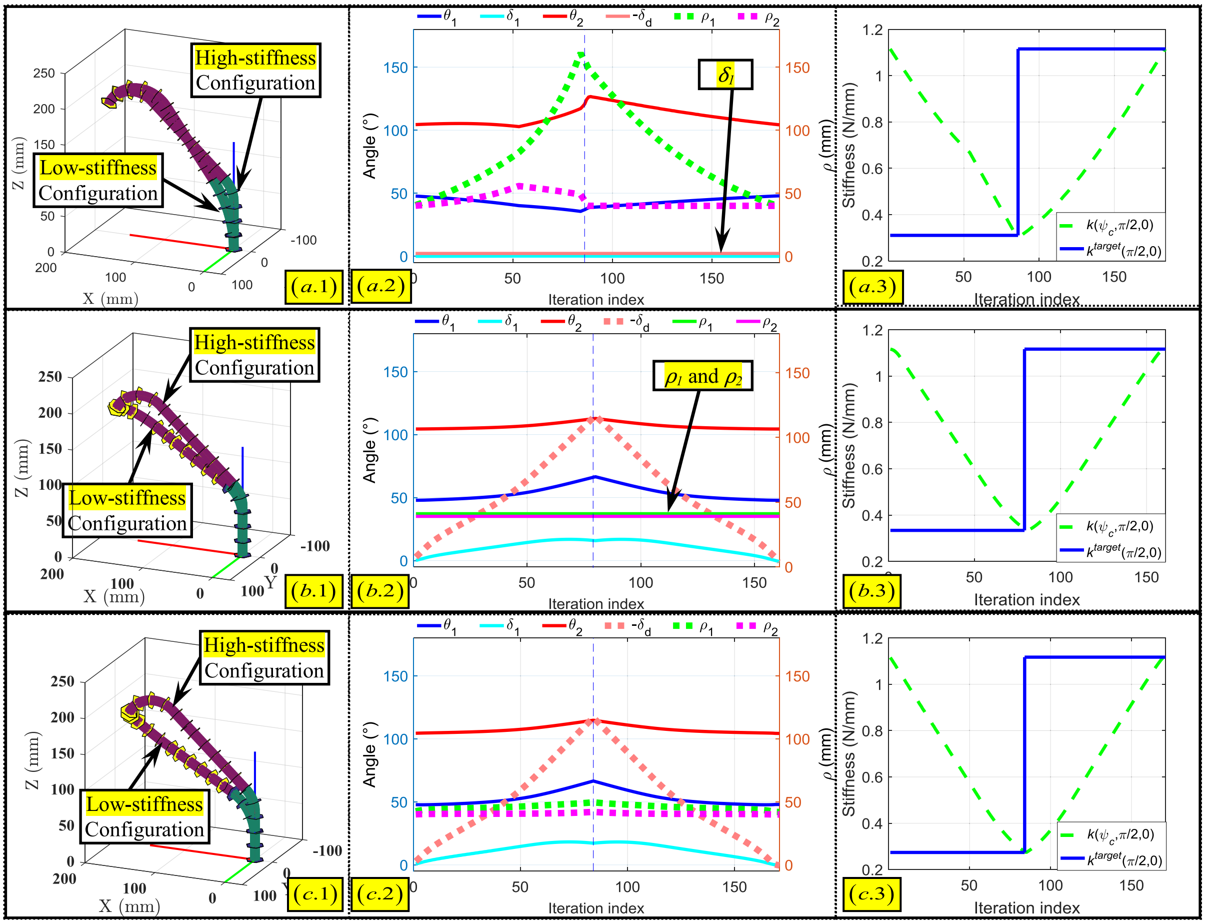

Fig. 10. Numerical experiments of stiffness control formulation: (a.1) Case I, the tip stiffness is changed by varying ρ_i, (a.2) control space variation, and (a.3) the target and current tip stiffness variation $k(\boldsymbol{\psi}, \pi/2,0)$; (b.1) Case II, the stiffness is adjusted by changing δ_d, (b.2) control space variation, and (b.3) the target and current tip stiffness variation $k(\boldsymbol{\psi}, \pi/2,0)$; and (c.1) Case III, the stiffness is changed by varying $\boldsymbol{\psi}_c$, (c.2) control space variation, and (c.3) the target and current tip stiffness variation $k(\boldsymbol{\psi}, \pi/2,0)$.

Maximal tip stiffness and stiffness variation ratio of the proposed continuum manipulator were quantified at the points across the workspace. The stiffness variation ratio is the ratio between the maximal and minimal tip stiffness.

Since the workspace of the continuum manipulator is axially symmetric with respect to the Z axis, the points in the first quadrant of the XZ-plane in the workspace were investigated. At each point, the maximal and minimal tip stiffness can be searched via the proposed stiffness control formulation as in Section 5.2.

The results of the maximal tip stiffness and the stiffness variation ratios are depicted in Fig. 11.

As shown in Fig. 11, the highest tip stiffness $k(\boldsymbol{\psi}_c, \pi/2,0)$, with the 2nd segment being straight, rigid, and almost parallel to the desired tip stiffness direction (a.k.a., in the X direction), is 39.11 N/mm. As shown in the inset, the stiffness is high because the stiffness is primarily in the axial direction of the manipulator. When the manipulator is at the positions close to the Z axis, the stiffness is relatively low because the measured tip stiffness is in the lateral direction with lengthened segments.

The maximal stiffness variation ratio is 90.63, as shown in Fig. 11(b). The reason may be seen from the inset of Fig. 11(a). The maximal tip stiffness is in the axial direction of the manipulator. The manipulator can change its pose such that i) the stiffness direction is moved towards the manipulator's lateral direction, and ii) more importantly the bent segments are lengthened. Then, the directional stiffness is substantially reduced.

The stiffness variation ratio at the ${}^{1b}\mathbf{p}_D$ point in Fig. 11(b) is calculated as 12.02. The experimental verification showed a stiffness variation ratio of 10.83 as presented in Section 6.5.

6.5. Stiffness variation verification

With the motion compensation and calibration of stiffness parameters implemented, the stiffness variation was achieved by the proposed stiffness control formulation and carried out at different positions on the actual system. The goal of the experiment is to show the usefulness of the stiffness control formulation and the proposed design.

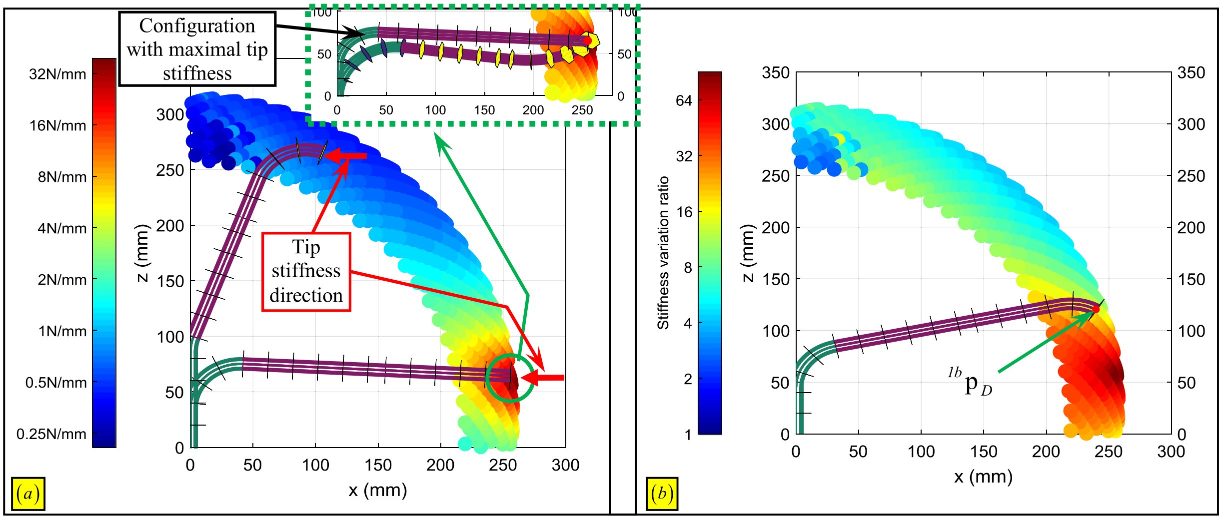

Fig. 11. Numerical experimental results: (a) maximal tip stiffness $k(\boldsymbol{\psi}_c, \pi/2{,}0)$, and (b) stiffness variation ratio.

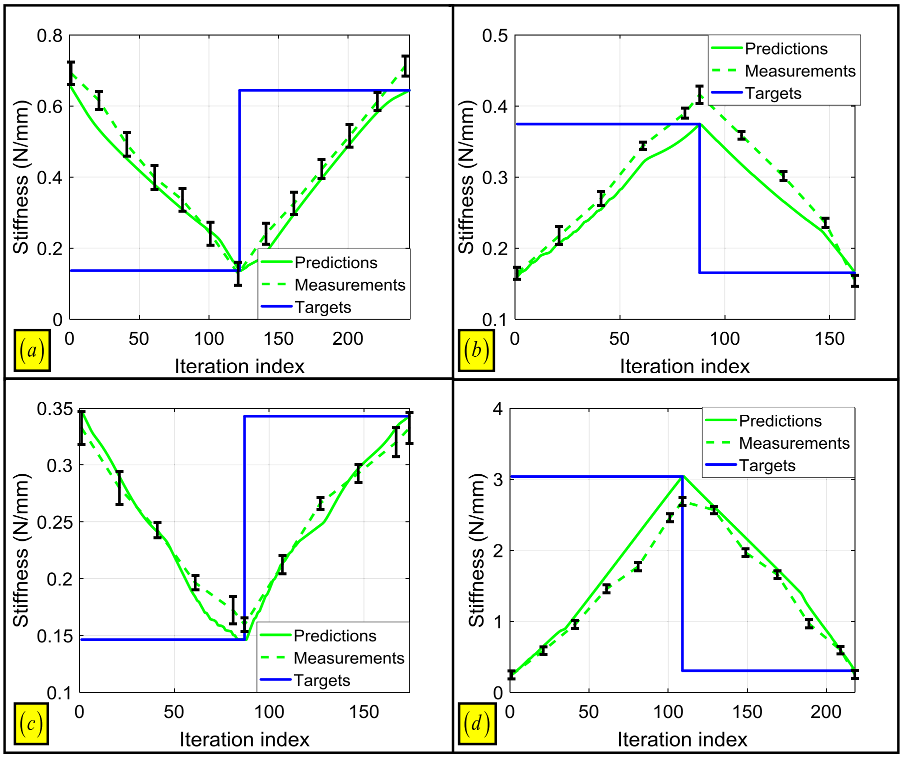

Fig. 12. Stiffness variation of the stiffness control formulation at (a) $^{1b}\mathbf{p}_A$ along the direction ($\pi/4$, $\pi/4$)·(b) $^{1b}\mathbf{p}_B$ along the direction ($\pi/2$, $\pi/4$), (c) $^{1b}\mathbf{p}_C$ along the direction (0, 0), and (d) $^{1b}\mathbf{p}_D$ along the direction ($\pi/2$, 0).

The 2-segment continuum manipulator was actuated to four positions (from $^{1b}\mathbf{p}_A$ to $^{1b}\mathbf{p}_D$, as shown in Fig. 7). For each target tip position, the continuum manipulator was driven by the stiffness control formulation to vary the tip stiffness while maintaining the tip position, and the tip stiffness is quantified in different directions (α, β). The verification would vary the continuum arm from the initial configuration, to the configuration with low or high stiffness, and back to the original configuration. During iterations of the stiffness control formulation, the stiffness of the manipulator is measured in a quasi-static condition every 20 iterations, using a similar setup as in Section 6.2. Fig. 12 plots the measured tip stiffness values from nine experiments and the predicted values of stiffness control formulation at the four positions in different directions. The tip stiffness was reduced at $^{1b}\mathbf{p}_A$ and $^{1b}\mathbf{p}_C$, and increased at $^{1b}\mathbf{p}_B$ and $^{1b}\mathbf{p}_D$.

The tip stiffness measurements and predictions are detailed in Fig. 12. Some observations can be made from the results.

- The discrepancy between the experimental tip stiffness and the predicted results is generally small. The discrepancy is believed to be from the model simplification that the continuum manipulator was regarded as a single rod.
- Tip stiffness of the continuum manipulator is decreased at ${}^{1b}\mathbf{p}_{\mathrm{A}}$ and ${}^{1b}\mathbf{p}_{\mathrm{C}}$, while tip stiffness is increased at ${}^{1b}\mathbf{p}_{\mathrm{B}}$ and ${}^{1b}\mathbf{p}_{\mathrm{D}}$. The results show that the trend of the measured tip stiffness is consistent with that of the predicted tip stiffness. Hence, the stiffness control formulation can be applied to adjust/control tip stiffness, even though the model simplification is not avoided.
- Among these cases, the tip stiffness of the final configuration is increased or decreased from 1.93 times in Fig. 12(c) to 10.83 times in Fig. 12(d) the initial values of the stiffness control formulation. Thus, the efficacy of the proposed design and the stiffness control formulation can achieve continuously variable stiffness.
- As shown in Fig. 12, it would take about 100 iterations for the stiffness to vary from the highest to the lowest or to the lowest to the highest. As a quick insertion or extraction of the curvature constraining rod would introduce disturbances to the shape, the stiffness variation time is set to 2 s for the stiffness from the highest to the lowest, and 3 s for the stiffness from the lowest to the highest.
- The experimental results show that the proposed approach does not bring noticeable hysteresis. The tip stiffness returned to the initial value after a cycle of variation.

7. Conclusions

Continuum manipulators have become popular in various applications in confined spaces because of their safe interactions and distal dexterity. They are at times expected to have adjustable stiffness to handle different tasks. Hence, the paper proposes a 2-segment continuum manipulator design with continuously variable stiffness for increasing its usefulness. The design utilizes the concepts of constraining bending curvature for stiffness variation and redundant backbone arrangement for stiffness enhancement. The proposed continuum manipulator has two serially connected DSs actuated by PSs, and the curvature-constraining rods are used to alter the effective length of the continuum segments. The joint chain with low flexural rigidity and high axial rigidity is a key component for actuating the CC rod-2 and enabling this proposed idea. The kinematics is derived by assuming a circular shape and that the effective segment length can be changed continuously. The manipulator is then approximately modeled as a single rod, and the Cosserat rod theory is applied in the kinestatic model to calculate the deflection of the manipulator. The tip stiffness is numerically obtained by solving the equations of the Cosserat rod theory. The stiffness control formulation fully utilizes the redundant configuration DoFs to adjust the tip stiffness in a desired direction while reaching a target tip position.

Experiments were carried out for motion compensation, stiffness parameter calibration, and stiffness control verifications. The results of the numerical experiments demonstrate that stiffness variation can be achieved by changing the radii of curvature ρ_i and the angle between the two segments' bending planes δ_d. The experiments of stiffness control verification show that the stiffness control formulation can be used to control the tip stiffness, even though there is a discrepancy between the experimental stiffness and the predicted stiffness. The results also show that the tip stiffness of the continuum manipulator can be enhanced 10.83 times.

Compared with the state-of-the-art approaches for stiffness variation, this proposed approach does not bring noticeable actuation hysteresis because the inserted components only change the structure's elastic bending behaviors. What's more, the inserted components are passive. It requires less change to the manipulator structures. On the other hand, the stiffness of the continuum manipulator is finite. The tip position can be disturbed under external and internal disturbance (e.g., insertion of the CC rod). What's more, How to design a curvature-constrained continuum manipulator with more than three segments is still challenging.

Declaration of Competing Interest

The authors declare that they have no known competing financial interests or personal relationships that could have appeared to influence the work reported in this paper.

Acknowledgments

This work was supported in part by the National Natural Science Foundation of China (Grant no. 51435010, Grant no. 51722507 and Grant no. 91648103).

References

[1] I.D. Walker, Continuous backbone "Continuum"; robot manipulators, ISRN Robot. 2013 (2013) 1–19.
[2] Z. Li, H. Ren, P.W.Y. Chiu, R. Du, H. Yu, A novel constrained wire-driven flexible mechanism and its kinematic analysis, Mech. Mach. Theory 95 (2016) 59–75.
[3] J. Burgner-Kahrs, D.C. Rucker, H. Choset, Continuum robots for medical applications: a survey, IEEE Trans. Robot. 31 (2015) 1261–1280.
[4] W. McMahan, V. Chitrakaran, M. Csencsits, D.M. Dawson, I.D. Walker, B.A. Jones, M. Pritts, D. Dienno, M. Grissom, C.D. Rahn, Field trials and testing of the octarm continuum manipulator, in: Proceedings of the IEEE International Conference on Advanced Robotics (ICAR), Orlando, FL, USA, 2006, pp. 2336–2341.

[5] E. Paljug, T. Ohm, S. Hayati, The JPL serpentine robot: a 12 DOF system for inspection, in: Proceedings of the IEEE International Conference on Robotics and Automation (ICRA), Washington, DC, 1995, pp. 3143–3148.
[6] R. Buckingham, A. Graham, Nuclear snake-arm robots, Ind. Robot.: Int. J. 39 (2012) 6–11.
[7] S. Liu, Z. Yang, Z. Zhu, L. Han, X. Zhu, K. Xu, Development of a dexterous continuum manipulator for exploration and inspection in confined spaces, Ind. Robot.: Int. J. 43 (2016) 284–295.
[8] V. Saadat, R.C. Ewers, E.G. Chen, Shape Lockable Apparatus and Method for Advancing an Instrument through Unsupported Anatomy, USGI Medical, Inc., US, 2004.
[9] A. Degani, H. Choset, A. Wolf, M.A. Zenati, Highly articulated robotic probe for minimally invasive surgery, in: Proceedings of the IEEE International Conference on Robotics and Automation (ICRA), Orlando, Florida, 2006, pp. 4167–4172.
[10] Y.-J. Kim, S. Cheng, S. Kim, K. Iagnemma, A stiffness-adjustable hyperredundant manipulator using a variable neutral-line mechanism for minimally invasive surgery, IEEE Trans. Robot. 30 (2014) 382–395.
[11] P.M. Loschak, S.F. Burke, E. Zumbro, A.R. Forelli, R.D. Howe, A robotic system for actively stiffening flexible manipulators, in: Proceedings of the IEEE/RSJ International Conference on Intelligent Robots and Systems (IROS), Hamburg, Germany, 2015, pp. 216–221.
[12] A.J. Loeve, O.S.v.d. Ven, J.G. Vogel, P. Breedveld, J. Dankelman, Vacuum packed particles as flexible endoscope guides with controllable rigidity, Granular Matter 12 (2010) 543–554.
[13] N.G. Cheng, M.B. Lobovsky, S.J. Keating, A.M. Setapen, K.I. Gero, A.E. Hosoi, K.D. Iagnemma, Design and analysis of a robust, low-cost, highly articulated manipulator enabled by jamming of granular media, in: Proceedings of the IEEE International Conference on Robotics and Automation (ICRA), Saint Paul, Minnesota, USA, 2012, pp. 4328–4333.
[14] Y.-J. Kim, S. Cheng, S. Kim, K. Iagnemma, A novel layer jamming mechanism with tunable stiffness capability for minimally invasive surgery, IEEE Trans. Robot. 29 (2013) 1031–1042.
[15] A. Yagi, K. Matsumiya, K. Masamune, H. Liao, T. Dohi, Rigid-Flexible outer sheath model using slider linkage locking mechanism and air pressure for endoscopic surgery, in: Proceedings of the International Conference on Medical Image Computing and Computer-Assisted Intervention (MICCAI), Copenhagen, Denmark, 2006, pp. 503–510.
[16] M.S. Moses, M.D.M. Kutzer, H. Ma, M. Armand, A continuum manipulator made of interlocking fibers, in: Proceedings of the IEEE International Conference on Robotics and Automation (ICRA), Karlsruhe, Germany, IEEE, 2013, pp. 4008–4015.
[17] B. Kang, R. Kojcev, E. Sinibaldi, The first interlaced continuum robot, devised to intrinsically follow the leader, PLoS ONE 11 (2016) e0150278.
[18] A. Pettersson, S. Davis, J.O. Gray, T.J. Dodd, T. Ohlsson, Design of a magnetorheological robot gripper for handling of delicate food products with varying shapes, J. Food Eng. 98 (2010) 332–338.
[19] A. Sadeghi, L. Beccai, B. Mazzolai, Innovative soft robots based on electro-rheological fluids, in: Proceedings of the IEEE/RSJ International Conference on Intelligent Robots and Systems (IROS), Vilamoura , Algarve, Portugal, 2012, pp. 4237–4242.
[20] Y. Kim, S.S. Cheng, J.P. Desai, Active stiffness tuning of a spring-based continuum robot for MRI-Guided neurosurgery, IEEE Trans. Robot. 34 (2017) 18–28.
[21] M.J. Telleria, M. Hansen, D. Campbell, A. Servi, M.L. Culpepper, Modeling and implementation of solder-activated joints for single-actuator, centimeter-scale robotic mechanisms, in: Proceedings of the IEEE International Conference on Robotics and Automation (ICRA), Anchorage, Alaska, USA, 2010, pp. 1681–1686.
[22] W. Shan, T. Lu, C. Majidi, Soft-matter composites with electrically tunable elastic rigidity, Smart Mater. Struct. 22 (2013) 1–8.
[23] J. Wang, S. Wang, J. Li, X. Ren, R.M. Briggs, Development of a novel robotic platform with controllable stiffness manipulation arms for laparoendoscopic single-site surgery (LESS), Int. J. Med. Robot. Comput. Assis. Surg. EarlyView (2017) e1838.
[24] M. Mahvash, P.E. Dupont, Stiffness control of surgical continuum manipulators, IEEE Trans. Robot. 27 (2011) 334–345.
[25] D.C. Rucker, R.J. Webster, Statics and dynamics of continuum robots with general tendon routing and external loading, IEEE Trans. Robot. 27 (2011) 1033–1044.
[26] W.S. Rone, P. Ben-Tzvi, Continuum robot dynamics utilizing the principle of virtual power, IEEE Trans. Robot. 30 (2014) 275–287.
[27] A. Bajo, N. Simaan, Hybrid motion/force control of multi-backbone continuum robots, Int. J. Robot. Res. OnlineFirst (2015) 1–13.
[28] K. Xu, N. Simaan, An investigation of the intrinsic force sensing capabilities of continuum robots, IEEE Trans. Robot. 24 (2008) 576–587.
[29] K. Xu, N. Simaan, Intrinsic wrench estimation and its performance index of multi-segment continuum robots, IEEE Trans. Robot. 26 (2010) 555–561.
[30] C.B. Black, J. Till, D.C. Rucker, Parallel Continuum Robots, Modeling, analysis, and actuation-based force sensing, IEEE Trans. Robot. 34 (2018) 29–47.
[31] M.L. Fugoso, D.H. Tran, Adjustable Stiffness Dilatation Catheter, Medtronic, Inc., US, 1996.
[32] B.L. Conrad, J. Jung, R.S. Penning, M.R. Zinn, Interleaved continuum-rigid manipulation: an augmented approach for robotic minimally-invasive flexible catheter-based procedures, in: Proceedings of the IEEE International Conference on Robotics and Automation (ICRA), Karlsruhe, Germany, 2013, pp. 718–724.
[33] K. Xu, M. Fu, J. Zhao, An experimental kinestatic comparison between continuum manipulators with structural variations, in: Proceedings of the IEEE International Conference on Robotics and Automation (ICRA), Hong Kong, China, 2014, pp. 3258–3264.
[34] B. Zhao, W. Zhang, Z. Zhang, X. Zhu, K. Xu, Continuum manipulator with redundant backbones and constrained bending curvature for continuously variable stiffness, in: Proceedings of the IEEE/RSJ International Conference on Intelligent Robots and Systems (IROS), Madrid, Spain, 2018, pp. 7492–7499.
[35] K. Xu, J. Zhao, M. Fu, Development of the sjtu unfoldable robotic system (SURS) for single port laparoscopy, IEEE/ASME Trans. Mechatron. 20 (2015) 2133–2145.
[36] K. Xu, N. Simaan, Analytic formulation for the kinematics, statics and shape restoration of multibackbone continuum robots via elliptic integrals, J. Mech. Robot. 2 (2010) 1–13.
[37] D.C. Rucker, B.A. Jones, R.J. Webster, A geometrically exact model for externally loaded concentric-tube continuum robots, IEEE Trans. Robot. 26 (2010) 769–780.
[38] J. Till, C.E. Bryson, S. Chung, A. Orekhov, D.C. Rucker, Efficient computation of multiple coupled cosserat rod models for real-time simulation and control of parallel continuum manipulators, in: Proceedings of the IEEE International Conference on Robotics and Automation (ICRA), Seattle, Washington, 2015, pp. 5067–5074.
[39] K. Xu, N. Simaan, Actuation compensation for flexible surgical snake-like robots with redundant remote actuation, in: Proceedings of the IEEE International Conference on Robotics and Automation (ICRA), Orlando, Florida, USA, 2006, pp. 4148–4154.